

Nanosized Electrochemical Cells Operated by AFM Conducting Probes

Olivier Schneegans,[†] Alec Moradpour,^{*,‡} Lionel Boyer,^{†,§} and Dominique Ballutaud^{||}

Laboratoire du Génie Electrique de Paris, UMR 8507 of CNRS, Paris VI and Paris-Sud Universities, Supélec, F-91192 Gif-sur-Yvette Cedex, France, Laboratoire de Physique des Solides, UMR C8502 of CNRS, University Paris-Sud, F-91405 Orsay Cedex, France, and Laboratoire de Physique des Solides et Cristallogénèse, UMR 8635 of CNRS, University of Versailles, F-78035 Versailles, France

Received: March 24, 2004; In Final Form: April 30, 2004

The study of the conducting-probe atomic force microscopy (AFM) ambient-air nanopatterning of a molecular conducting single crystal is reported. The implication of electrochemical reactions both in the substrate modification, which yield nanometer-scale insulating regions, and in the conducting-probe-mediated complementary water redox reaction is demonstrated. The rate of the process controlling the dimension of the resulting insulating regions is mainly controlled by the conducting-probe potential. The faradaic currents are found to be exceedingly low as compared to the total current flowing in the AFM probe contact-junction and a proposed model validates this feature.

Introduction

Conductive probe atomic force microscopy (CP-AFM) developed in the past decade, offers several distinct opportunities to characterize and pattern conductive materials on nanometer scales. The CP-AFM instruments allow one to simultaneously investigate the surface topography and the transport properties of materials. Moreover, the topographical imaging is controlled solely by contact forces and is therefore independent of the voltage bias required for the transport-measurement processes. Two kinds of measurements are basically achievable with these instruments: stationary-point electrical contact measurements and surface resistance maps.¹ Recently, stationary-point CP-AFM contact measurements have been used to probe molecular junctions, either with SAM of alkanethiols,² unsaturated oligophenylene thiolates,³ or conjugated thiols dispersed into alkanethiols⁴ or to estimate molecular electron transport properties using the recently developed single molecule to metal “contact pads” approach.⁵ On the other hand, interesting resistance maps have for example been recorded for nanometer-scale InAs quantum dots,⁶ YBaCuO^{7a} and TiO₂ thin films,^{7b} and carbon nanotubes.^{7c}

Besides these interesting measurements, nanometer-scale surface modifications involving conducting-probe AFM-mediated processes have also been investigated.^{8–13} In fact, when working in ambient air, capillary water meniscus forms at the contact point of the conductive tip with the material, and a two-electrode electrochemical nanocell is supposed to be created therein. Various electrochemical processes might therefore be considered to proceed in this nano-cell and result in material surface patterning on nanometer scales. These include electrochemical “dip-pen” nanolithography (DPN),⁸ local oxidations of inorganic semiconductors—for example silicon^{9,10} and GaAs¹¹—as well as electrostatic polymer nanolithography,^{12a} cathodic alkynes electrografting on silicon surfaces,^{12b} or the newly invented method referred to as constructive nanolithography.^{12c}

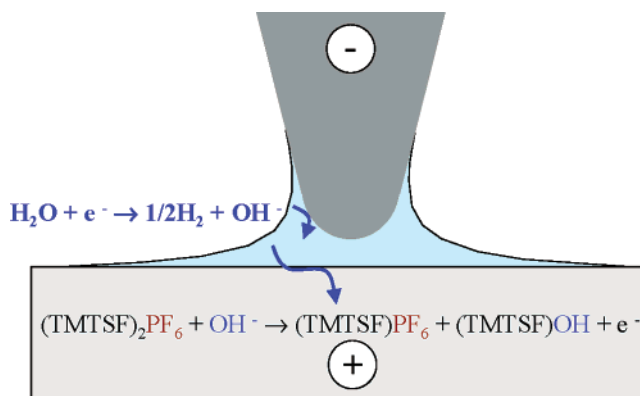


Figure 1. Illustration of the CP-AFM probe–substrate vicinity involving a water-meniscus nanocell.¹⁴ The electrochemical reactions are related to the “oxidative mode” and therefore involve the anodic oxidation of (TMTSF)₂PF₆ and the water-reduction reaction occurring simultaneously on the (tip) cathode; see the text.

We have recently described¹³ the first CP-AFM-mediated nanopatterning of molecular conducting materials. Using (TMTSF)₂PF₆ (TMTSF: tetramethyltetraselenafulvalene) as an example, we have reported the creation of nanometer-scale insulating regions on the (001) *ab* face of these conducting single crystals. The occurrence of electrochemical reactions as a source of these modifications was clearly indicated by the unsymmetric nature of the processes as a function of the tip-to-substrate bias direction: smooth nanometer-scale insulating barriers were obtained only with the instrument working in the (substrate) oxidative mode. In this case, the process and the corresponding electrochemical reactions¹⁴ are represented schematically in Figure 1.

In our initial work, we emphasized the importance of the crystal-to-probe working bias and showed that the width of the created insulating lines increase significantly with increasing bias potential. To assess more broadly the potential of this procedure, we report in this work a detailed study of the specific characteristics of these reactions, confined in the water-meniscus nanocells beneath the AFM probe apex. We report X-ray photoelectron spectroscopy (XPS) measurements of the oxidized

* Corresponding author. E-mail: moradpour@lps.u-psud.fr.

[†] Laboratoire du Génie Electrique de Paris.

[‡] Laboratoire de Physique des Solides.

[§] Deceased.

^{||} Laboratoire de Physique des Solides et Cristallogénèse.

insulating material obtained by this faradaic process, which demonstrate the influx of OH^- into these modified areas. Moreover, based on an analysis of the current potential curves investigated as a function of the potential scan rates, the occurrence of the associated water-reduction reaction is demonstrated by the use of platinum-coated probes in place of the previously investigated conducting diamond ones. We have also investigated the influence of the ambient humidity (in the 3–80% range) on the creation of the insulating patterns. Surprisingly, and although an effect of humidity on AFM-mediated surface modifications has previously been claimed, we find no significant influence of humidity on our surface modifications. We also demonstrate that only a small fraction of the extremely high current densities flowing through the probe contact point corresponds (in the ppm range) to faradaic currents. These results therefore provide a rational insight into this unique process directed to nanopatterning of the investigated conducting solids, and furthermore provide a general insight into such processes for other materials.

Experimental Section

(TMTSF) $_2$ PF $_6$ single crystals were prepared as previously described.¹⁵ Fractions of a typical crystal (6 mm \times 1 mm \times 0.3 mm) fixed by silver paste on steel disks were used for the study. A homemade system for local contact resistances and current measurements (Resiscope) derived from a Nanoscope III AFM instrument (Veeco) was utilized. When a bias voltage V ($-10 < V < 10$) is applied between the probe and the sample, the Resiscope allows currents ranging from 1 mA to almost 1 pA to be measured. For electrical image acquisitions, the sample was positively biased ($V = +1$ V). For the surface modification reactions, distinct voltage values (up to +9.8 V) were applied. One-legged diamond and Pt/Ir-coated Si cantilevers (Nanosensors, spring constant ≈ 2 N/m for diamond-coated and ≈ 0.1 N/m for Pt/Ir-coated cantilevers) were used (see note 21 in ref 13 for diamond-coated tip-performance improvements, whereas the platinum-coated cantilevers are much more easily damaged and require careful use to yield reproducible results). The reported surface modifications obtained with low tip-applied forces have been investigated in ambient air with a 45% relative humidity (at 25 $^\circ\text{C}$) and in humidity-controlled atmospheres. The surfaces of the insulating spots have been determined by computing the number of pixels corresponding to a resistance higher than $10^9 \Omega$. In a typical experiment, the cavity containing the AFM and the Resiscope was flushed for 2 h with dry nitrogen prior to the measurements; this procedure allowed us to determine the lowest explored humidity value (3% at 25 $^\circ\text{C}$). The humidity was also adjusted to 80% (at 25 $^\circ\text{C}$) by introducing water vapor into the cavity by bubbling nitrogen through a convenient water container.

XPS analysis was made on a VG ESCALAB 220i XL apparatus using the monochromatized Al K α X-ray source on 50 μm wide areas of the native and AFM-modified (TMTSF) $_2$ PF $_6$ single crystals. The binding energies were referenced to the C 1s peak at 285 eV. The 50 μm wide AFM-modified insulating regions were obtained by 10 μm wide consecutive scans using a +6 V bias diamond-probe voltage.¹⁶

Numerical simulations of the current–potential curves related to the constructed model were computed using the simulation program¹⁶ within a personal computer.

Results and Discussion

A. Current–Potential Curves. The crystal-to-probe current–potential (i/V) curves have been investigated. A typical

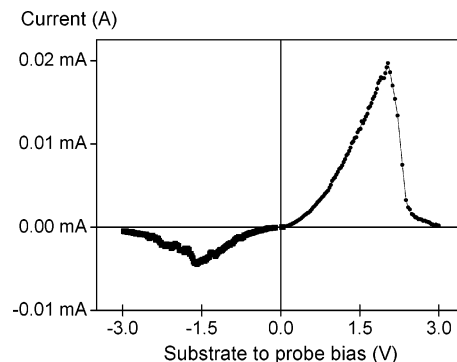


Figure 2. Current–potential diagram of a (TMTSF) $_2$ PF $_6$ single crystal obtained using a conducting diamond probe.

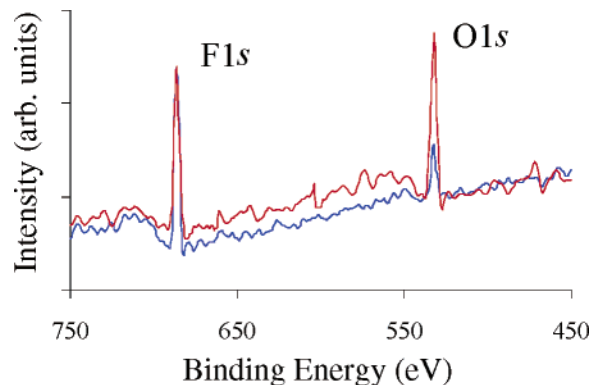
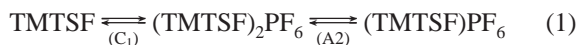


Figure 3. XPS spectra of the F 1s and O 1s core levels of native and AFM probe-modified areas of a (TMTSF) $_2$ PF $_6$ single crystal. The spectra are normalized considering the F 1s lines of both the native (in blue) and electrochemically modified (in red) areas.

(i/V) diagram of a (TMTSF) $_2$ PF $_6$ conductor obtained with a diamond probe is shown in Figure 2. The current is measured in the 20 μA range and corresponds to remarkably high current densities at the probe contact point.¹⁷

Two waves reminiscent of those corresponding to adsorbed electroactive species are detected.¹⁸ These electrochemical processes are attributed to the following reactions:



The reduction of (TMTSF) $_2$ PF $_6$ into neutral TMTSF, as well as the oxidation of these materials into 1:1 salts, has previously been investigated in the solid state within carbon paste electrode.¹⁹ The stoichiometry of oxidized (TMTSF)PF $_6$ 1:1 solid has been established by coulometry,¹⁹ although full characterization of such (unavailable) solids²⁰ had not been attempted in the past. Therefore, an XPS characterization of these oxidized areas was carried out, and before going into the detailed investigations of the crystal-to-probe current–potential curves of (TMTSF) $_2$ PF $_6$, the corresponding results are considered here.

In contrast to electrochemical studies, no electrolyte is presently involved in the water-meniscus nanocell, and the involvement of OH^- resulting in a (TMTSF) $_2$ (PF $_6$)(OH) 1:1 oxidized material was conjectured and investigated by XPS. Considering the F 1s and O 1s core level lines, observed respectively at binding energies of about 685 and 532 eV, the normalized spectra—with respect to the F 1s lines—for both the native surfaces and the oxidized areas are shown in Figure 3. A dramatic increase of the oxygen 1s line is observed, as compared to the residual (possibly due to contamination) oxygen 1s signal detected on the unmodified surfaces. Although a

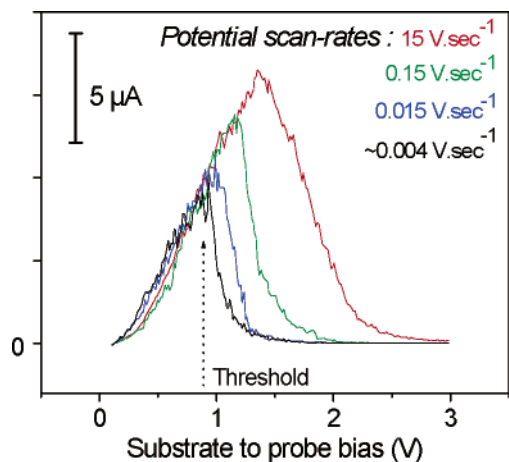


Figure 4. Current–potential diagrams of a (TMTSF)₂PF₆ single crystal investigated as a function of the potential scan rates (using a conducting diamond probe).

quantitative analysis of the modified regions' composition from these XPS spectra is impossible—as observed in a very recent XPS study of (TMTSF)₂PF₆ single crystals²¹—our results are in qualitative agreement with the expected influx of OH[−] into the oxidized areas.

Going back again to the current–potential diagram of a (TMTSF)₂PF₆ obtained with the CP-AFM instrument (Figure 2), the peak potential separation (over 2 V) is rather large when compared to the peak potentials $E_{pC1} = -0.03$ V and $E_{pA2} = +0.47$ V (vs SCE) determined by the carbon paste electrode technique for these reactions (eq 1),¹⁹ and clearly reflects a more intricate process involving associated water redox reactions. One such reaction couple—namely, the water reduction occurring at the AFM probe associated with the (TMTSF)₂PF₆ oxidation reaction—is schematized in the Figure 1.

This oxidation wave was first investigated as a function of potential scan rates,²² and remarkable “potential shifts” are achieved as a function of the scan rates (Figure 4). Decreasing the scan rates results in a set of (*i*/V) curves (Figure 4) exhibiting a *drastic decrease of the peak–current potential*. In addition, the different peak–current values apparently decrease (from right to left) along a pathway defined by overlapping fractions of the different voltammograms. Moreover, while potential scan rates are decreased to about 2×10^{-4} V·s^{−1}, the peak–current reaches a limiting value.²³ This result supports a *potential-dependent* phenomenon, and clearly points toward electrochemical processes involving potential thresholds. The threshold is presently estimated to be $V = E_{TH} = 0.9$ V, and corresponds to the lowest peak–current determined at 2×10^{-4} V·s^{−1}.

These electrochemical reactions involve a “sacrificial” oxidation of the (TMTSF)₂PF₆ anode and the coupled water-reduction half-reaction occurring on the conducting-probe electrode (Figure 1). Therefore, this potential threshold should mainly (if not exclusively) reflect the hydrogen formation overpotential of the probe's material. Consequently, the conversion of the conducting probe coating from diamond to platinum should significantly decrease this overpotential and the corresponding threshold.

As compared to the previous value obtained with diamond-coated probes ($E_{TH} = 0.9$ V), the (*i*/V) diagrams investigated as a function of the potential-scan rate with a Pt/Ir-coated conducting probe (Figure 5) clearly exhibit a lower potential threshold, found to be $V = E_{TH} = 0.6$ V. This result demonstrates that the expected water-reduction electrochemical reaction does indeed occur.

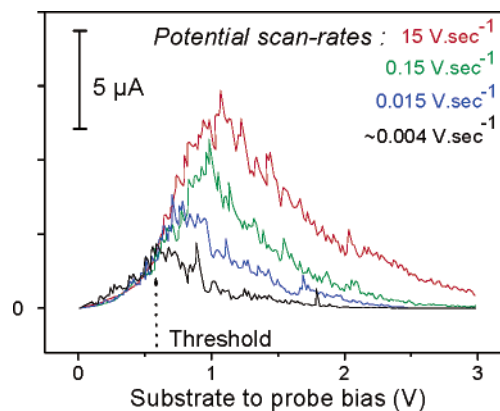


Figure 5. Current–potential diagrams of a (TMTSF)₂PF₆ single crystal investigated as a function of the potential scan rates (using a conducting Pt/Ir-coated probe).

If we now consider the potential range before the threshold is attained—for both (Figure 4 and 5) groups of (*i*/V) curves—the corresponding fractions of voltammograms almost overlap. Taking into account the rather large potential scan-rate range (almost four decades) presently investigated, the occurrence of any significant capacitive charging effect can be excluded, based on this overlap. The shared fractions of these curves correspond to the expected (nonohmic) behavior of a semiconductor-to-metal (probe-to-(TMTSF)₂PF₆) contact junction and involve a potential range where the material is electrochemically inactive: the “background-current” range. Above the potential threshold an electrochemical cell starts to operate and yields an insulator which terminates the probe–substrate current. Therefore, the present voltammograms result from the combination of a probe-to-substrate contact junction with an electrochemical potential-dependent faradaic nanocell. In other words, two distinct overlaid electrical currents (junction and faradaic) exist and might account (vide infra) for the extremely high current densities¹⁷ involved at the contact point.

B. Pulsed Experiments. To obtain more detailed insight into these processes and to evaluate the faradaic fraction of the total current, the local oxidation process within such nanocells is investigated by applying a *pulsed potential*.

The pulse duration is increased from 0.1 to 160 ms with the probe moving to a new position before each pulse, and the applied voltage is then varied between 2 and 9.8 V for each series of pulses. The resulting collection of insulating dots and the corresponding surfaces plotted versus time are shown in Figure 6a,b, respectively.

The surfaces of these insulating plots, which reflect the rates of the process, expand rapidly with the pulse durations, and are significantly enhanced with increasing potential (from 2 to 8 V). For pulses shorter than 2 ms, initially fast-growing rates are observed for all investigated potentials. For longer pulse durations the rates decrease almost uniformly for all potentials. An additional illustration of the high potential dependence of the insulating dot formations comes from the lowest potential results. Using a 2 V bias, the generation of insulating dots is only detected for current pulses longer than 100 ms, whereas for 3V almost 3 orders of magnitude shorter pulses (0.1 ms) yield detectable dots. Also, this potential-dependent phenomenon²⁴ probably reflects the size of the smallest presently detectable dot, estimated to almost 300 nm².

Dot formation allows us to estimate the corresponding faradaic currents along with the measurement of the total current passed through the probe substrate contact. Thus, for 0.1 s pulses (yielding 60 nm diameter spots at 4 V, Figure 6b) the total

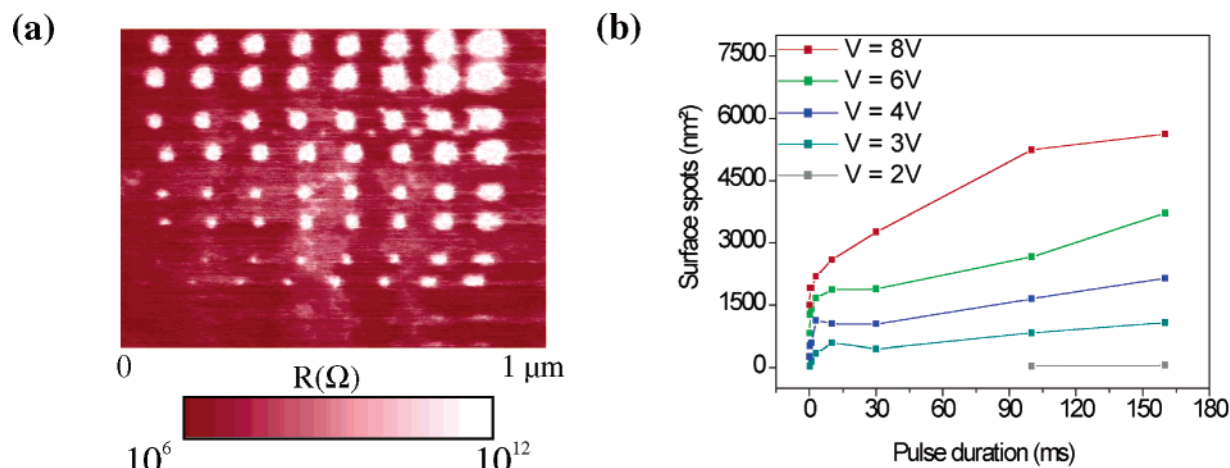


Figure 6. (a) Conductivity map of a $(\text{TMTSF})_2\text{PF}_6$ single crystal modified by pulsed voltages (2–8 V from down to up, respectively), as a function of the pulse durations (respectively 2–160 ms, from left to right). A conducting diamond probe is used for both the modifications and the imaging. (b) The corresponding insulating-dot surfaces are plotted as a function of the pulse duration.²⁴

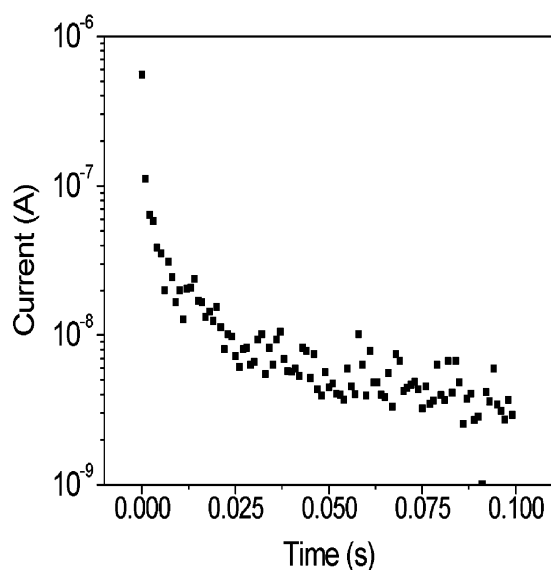


Figure 7. Total current passed through the probe–substrate contact recorded for a 0.1 s pulse at 4 V. This is given by $\int i \, dt = 1.6 \times 10^{-9}$ C.

recorded current is shown in Figure 7. The integral of the current versus time, which specify the total charge passed through the contact point, is around 1.6×10^{-9} C. Assuming the thickness of such an insulating spot to be 10 nm, the charge needed to

obtain it corresponds to only 3.6×10^{-15} C.²⁵ The order of magnitude of the total-to-faradaic current ratio is therefore estimated to be around 0.4×10^6 , indicating that the current is due, almost exclusively, to the probe-to-substrate junction current.

We have also investigated a possible role of humidity on the size of the spots generated by the pulsed bias. The influence of humidity on CP-AFM-mediated nanolithography has previously been observed for local oxidations of silicon,^{9b,26} and has been investigated in detail for DPN²⁷ In the latter case, an important effect of humidity was observed on the patterns' growth rates for some representative "inks".²⁷ Decreasing the ambient humidity causes a reduction of the width (by a factor of 4) of oxide lines created by the tip-induced oxidations, as claimed for silicon local oxidations.²⁶

Our results obtained with 6V bias after a careful flushing of the AFM apparatus with dry nitrogen to a 3% remaining humidity (at 25 °C) are reported in Figure 8. By contrast to the previous results of the silicon-oxidation investigations,^{9b,26} a surprisingly smaller effect (within 20% of the surface modification) is observed in the present study, decreasing the humidity to 3%.²⁸ The fact that capillary forces drive the residual water to the probe–substrate contact, and result in meniscus formation even under similar "dry" conditions, has been previously demonstrated.²⁷ Likewise, our results indicate that a water meniscus is still present on the substrate in such a dry medium

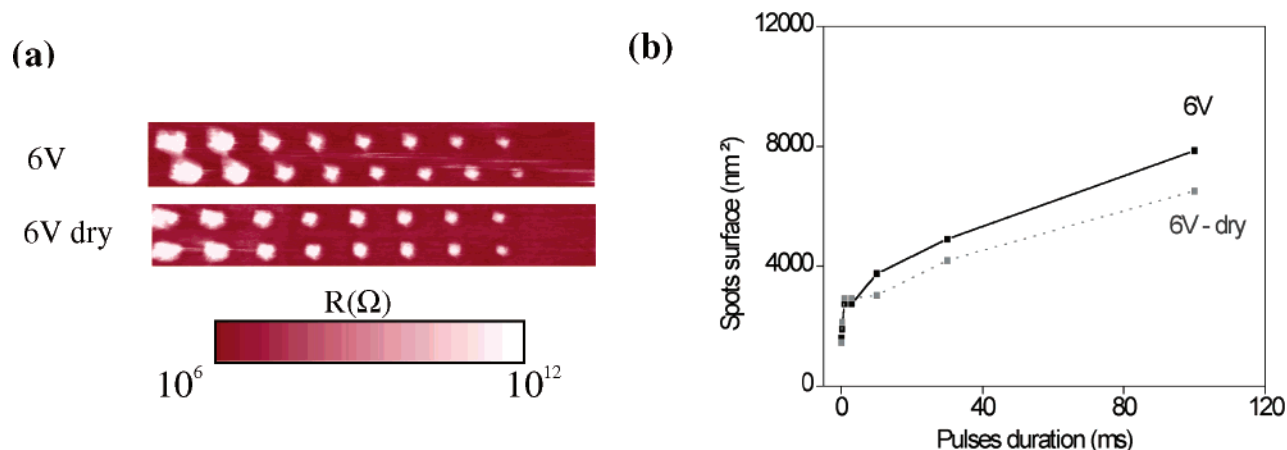


Figure 8. Influence of humidity on the insulating spot formations as a function of the bias pulse duration at 6 V: (a) conductivity map of the spots obtained in ambient humidity (45% at 25 °C) and in a "dry" atmosphere (remaining humidity of 3% at 25 °C); (b) the corresponding increase of the spot's surfaces plotted as a function of time.

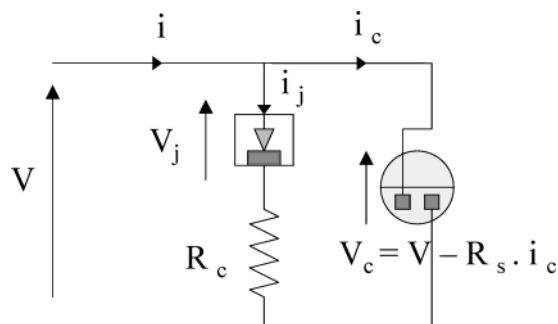


Figure 9. Model involving a probe–substrate considered for digital simulations of the CP-AFM surface-modification process. The circuit elements include a contact junction and an electrochemical cell in parallel ($i_c = 0$ if $V_c < E_{TH}$); for definitions of various resistances and applied potentials, see the text.

and that the size of such a meniscus does not interfere with the extension of the electrochemically modified areas. This is an indication that the dimensions of the modified areas are probably much smaller—even in “dry” media—than the surface of such a water meniscus, as also shown by the unmodified spot surfaces when humidity is increased to 80%.

C. Model for the Conducting Probe Current–Potential Behavior. To account for these results, we propose a model and calculate the current–potential characteristics of the overall process by digital simulations. The model, involving a probe–substrate contact junction and an electrochemical cell in parallel, is represented by the circuit elements in Figure 9. We assume here that (i) before the electrochemical threshold potential E_{TH} is attained (nonoperating cell), the (i/V) dependence fits a parabolic relationship and that the junction current is given by $i_j = K_1(V_j)^2$; (ii) at a fresh contact point, the initial resistance corresponds to the probe–substrate junction resistance. Above the potential threshold $V \geq E_{TH}$, an additional faradaic current i_c is established across the cell and yields a current-dependent amount of insulating material (M_c) from the conducting organic material given by $M_c = K_2 \int i_c dt$. The corresponding electrochemically generated additional resistance R_c is estimated to be $R_c = K_3[\exp(M_c) - 1]$, and eventually interrupts the junction current. To represent the electrochemical nanocell, a capacity might also be associated with this resistance R_c . Nevertheless, in the present we have not taken into account this capacity since we find that the overall probe–substrate process is already well-

simulated by only considering the resistance generated by the faradaic current (vide infra).

The decrease of the ionic current throughout an electrochemically grown insulating layer on an electrode, and therefore the decrease of the faradaic current, is commonly assumed²⁹ to be related to a continuous decrease of the movement of ions across this “passive” layer. This is due to the decrease of the electric field strength that controls the movement of ions across the growing oxidized layer under potentiostatic conditions. Hence, in a fashion similar to models previously advanced to account for the kinetics of anodic oxide films on metals,²⁹ the faradaic current i_c generating M_c is presently assumed to be

$$i_c = K_5[\exp(K_4(V - E_{TH})/M_c) - 1]; \quad i_c = 0 \text{ for } V < E_{TH}$$

Using these variables, the current–potential dependence, $i = f(V)$, is computed³⁰ by means of the following equations:

$$i = i_j + i_c$$

$$V = V_j + R_c i_j$$

$V = V_c + R_s i_c$ (the voltage V applied to the nanocell is distributed in an electrochemical potential and an ohmic drop due to a resistance R_s , representing the nanocell and the ion-flow resistances,²⁹ respectively). This model was used to simulate (i) the probe–substrate current–potential behavior as a function of potential scan rate and (ii) the kinetics of the insulating-material formation as a function of the probe’s bias. The simulated diagrams are shown respectively in (Figure 10a,b). Both sets of simulated curves fit fairly well to the experimental results. The shape and the essential features of the experimental (i/V) curves determined as a function of the potential scan rate (compare Figures 4 and 10a), as well as the rate of the process as illustrated by the surfaces of the insulating plots measured versus time for various probe bias (compare Figures 6b and 10b), are well-reproduced and substantiate the model’s underlying assumptions. The main features of this model include the existence of two overlying currents resulting from a contact junction and an electrochemical nanocell, combined in parallel, as well as an ionic current control of the anodic insulating-film growth.

In summary, the work reported in this paper provides a detailed insight into the processes involved in ambient air

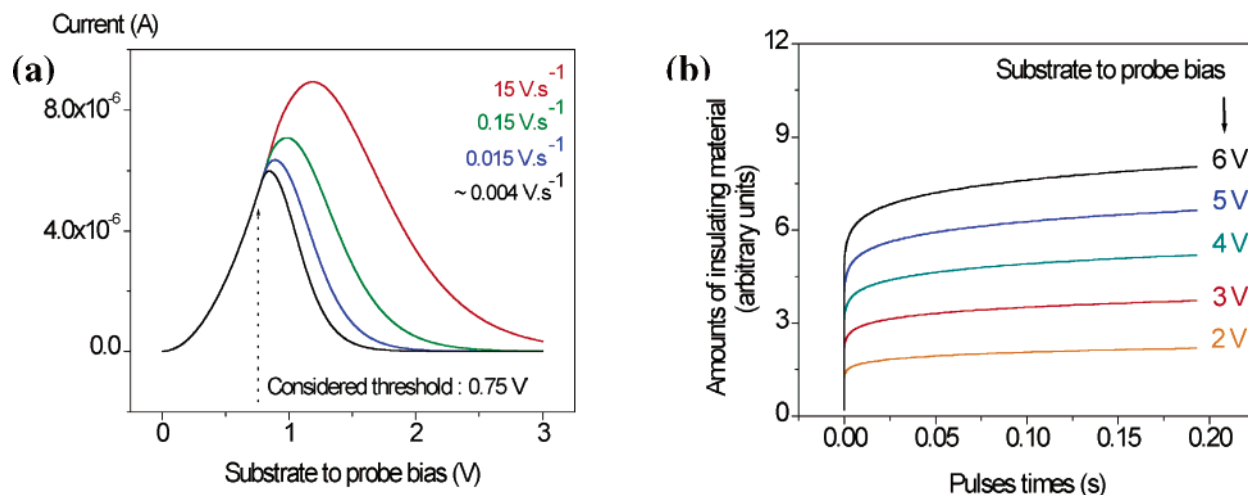


Figure 10. Simulated curves of (a) probe–substrate current–potential behavior as a function of potential scan rates and (b) the amounts of insulating material formed as a function of time for different probe’s bias, using the model depicted in Figure 9. The simulations are obtained²⁷ considering an electrochemical potential threshold of 0.75 V.

conducting-probe AFM surface modifications of conducting molecular materials. We have demonstrated that electrochemical reactions are implicated both in the substrate modification and in the conducting-probe-mediated complementary water redox reaction. The reaction rates and the size of the resulting insulating regions are mainly controlled by the probe's potential, and the effect of the ambient-humidity changes on the shape of the patterns is minor. The faradaic currents involved in this process are determined to be exceedingly low as compared to the total current flowing in the AFM probe contact junction and our proposed model validates this feature. Consequently, other fascinating yet uninvestigated potential uses of CP-AFM might be anticipated beyond the presently investigated electrochemical nanopatterning of conducting materials. As a matter of fact, the extremely high current densities¹⁷ implicated in the contact junction—and the possible thermal effects resulting therefrom—might also involve new specific and useful outcomes using suitable substrates. We are currently working in this direction.³¹

Supporting Information Available: Details on the optical visualization of the electrochemically modified areas and the algorithms and the corresponding listings used in numerical simulations. This material is available free of charge via the Internet at <http://www.pubs.acs.org>.

References and Notes

- (1) Kelley, T. W.; Granstrom, E. L.; Frisbie, C. D. *Adv. Mater.* **1999**, *11*, 261, and references therein.
- (2) Wold, D. J.; Frisbie, C. D. *J. Am. Chem. Soc.* **2001**, *123*, 5549.
- (3) Wold, D. J.; Haag, R.; Rampi, M. A.; Frisbie, C. D. *J. Phys. Chem. B* **2002**, *106*, 2813.
- (4) Ishida, T.; Mizutani, W.; Aya, H.; Ogiso, H.; Sasaki, S.; Tokumoto, H. *J. Phys. Chem. B* **2002**, *106*, 5886.
- (5) (a) Cui, X. D.; Primak, A.; Zarate, X.; Tomfohr, J.; Sankey, O. F.; Moore, A. L.; Moore, T. A.; Gust, D.; Nagahara, L. A.; Lindsay, S. M. *J. Phys. Chem. B* **2002**, *106*, 8609. (b) Ramachandran, G. K.; Tomfohr, J. K.; Li, J.; Sankey, O. F.; Zarate, X.; Primak, A.; Terazono, Y.; Moore, T. A.; Moore, A. L.; Gust, D.; Nagahara, L. A.; Lindsay, S. M. *J. Phys. Chem. B* **2003**, *107*, 6162.
- (6) Tanaka, I.; Kamiya, I.; Sakaki, H.; Qureshi, N.; Allen, S. J., Jr.; Petroff, P. M. *Appl. Phys. Lett.* **1999**, *74*, 844.
- (7) See: (a) Dégardin, A. F.; Schneegans, O.; Houzé, F.; Caristan, E.; DeLuca, A.; Chrétien, P.; Boyer, L.; Kreisler, A. *J. Physica C* **2000**, *341–348*, 1965. (b) Boxley, C. J.; White, H. S.; Gardner, C. E.; Macpherson, J. V. *J. Phys. Chem. B* **2003**, *107*, 9677. (c) Dai, H.; Wong, E. W.; Liebert, M., *Science* **1996**, *272*, 523.
- (8) (a) Li, Y.; Maynor, B. W.; Liu, J. *J. Am. Chem. Soc.* **2001**, *123*, 2105. (b) Agarwal, G.; Naik, R. R.; Stone, M. O., *J. Am. Chem. Soc.* **2003**, *125*, 7408.
- (9) (a) Avouris, P.; Hertel, T.; Martel, R. *Appl. Phys. Lett.* **1997**, *71*, 285. (b) Bloess, H.; Staikov, G.; Schultze, J. W. *Electrochim. Acta*, **2001**, *47*, 335.
- (10) See also: Lee, W.; Kim, E. R.; Lee, H. *Langmuir* **2002**, *18*, 8375.
- (11) Okada, Y.; Amano, S.; Kawabe, M.; Harris, J. S., Jr. *J. Appl. Phys.* **1998**, *83*, 7998.
- (12) (a) Lyuksyutov, S. F.; Vaia, R. A.; Paramonov, P. B.; Juhl, S.; Waterhouse, L.; Ralich, R. M.; Sigalov, G.; Sancaktar, E. *Nature Materials*, **2003**, *2*, 468. (b) Hurley, P. T.; Ribbe, A. E.; Buriak, J. M. *J. Am. Chem. Soc.* **2003**, *125*, 11334; (c) Hoeppeener, S.; Maoz, R.; Sagiv, J. *Nano Lett.* **2003**, *6*, 761.
- (13) Schneegans, O.; Moradpour, A.; Houzé, F.; Angelova, A.; Henry de Villeneuve, C.; Allongue, P.; Chrétien, P. *J. Am. Chem. Soc.* **2001**, *123*, 11486.
- (14) This figure is not intended to be a substantial representation of the actual probe-substrate vicinity, but rather a sketch of the electrochemical cell elements and a summary of the electrode reactions. Actually, the AFM probe somehow contacts the sample, but a precise description of this contact—involving certainly few water layers between the probe and the substrate—is presently difficult. Moreover, it is worth noting that: (i) the probe-sample contact implies a current corresponding to such a junction, (ii) this junction-current (not schematized in this figure) is superimposed to the current corresponding to the faradaic process schematized here (see the text for the evaluation of these currents).
- (15) Angelova, A.; Moradpour, A.; Auban-Senzier, P.; Akaaboune, N.-E.; Pasquier, C. *Chem. Mater.* **2000**, *12*, 2306.
- (16) see: Supporting Information Available
- (17) Assuming the surface of the probe contact-point to be in the 10 nm² range this current involves current densities in the 10⁶ A per (mm)² range.
- (18) However, each wave is obtained only for the first forward scan; any subsequent scan at a fixed contact-point involves highly insulating contacts in both potential directions. The waves shown in Figure 2 are therefore recorded starting from zero bias, then changing the probe contact-point subsequently to each scan in either potential direction.
- (19) Lamache, M.; Wuryanto, S.; Benhamou, F. *Electrochim. Acta* **1985**, *30*, 817.
- (20) Only a single (solvent containing) TMTSF cation-radical 1: 1 perchlorate salt has ever been described, see: Kobayashi, H.; Kobayashi, A.; Sasaki, Y.; Saito, G.; Inokuchi, H. *Bull. Chem. Soc. Jpn.* **1983**, *56*, 2894.
- (21) The surface composition of native (TMTSF)₂ PF₆ single crystal determined by XPS is found to deviate substantially from the bulk composition, as reflected by very important and systematic relative deviations of the surface composition from the nominal composition of the bulk; this rules out any quantitative surface-composition determination by XPS; see: Sing, M.; Schwingenschlögl, U.; Claessen, R.; Dressel, M.; Jacobsen, C. S. *Phys. Rev. B* **2003**, *67*, 125402.
- (22) As previously reported in our preliminary communication,¹³ bias in the negative direction yield severe sample surface-damages, such as disconnections of conducting fragments, or even probe degradations. A complicated and rather scan-to-scan irreproducible (i/V) behavior is obtained in the negative potential range, probably reflecting the same phenomena, and therefore only the scan-rate dependence of the oxidation wave is reported here.
- (23) Subsequent voltammograms corresponding to scan rates slower than 2×10^{-4} V.sec⁻¹ overlap almost completely with the (i/V) curve corresponding to this limit.
- (24) This bias-dependent effect is also different from one probe to another, and possibly depends on the probe's apex sharpness. Thus for some probes, no detectable dots are obtained at 2V even with 160ms pulse durations, whereas the smallest detected surface modifications are by contrast observed with 3V bias. It is worth noting that such a tip to tip variation does not account for the difference in the onset potential between the diamond probes and the platinum ones, shown above (see Figures 4 and 5); in fact, the same onset potential is obtained reproducibly using various platinum and diamond probes.
- (25) $V=714.3 \text{ Å}^3$, ($Z=1$), see: Thorup, N.; Rindorf, G.; Soling, H.; Bechgaard, K. *Acta Cryst.* **1981**, B37, 1236.
- (26) Avouris, P.; Martel, R.; Hertel, T.; Sandsrom, R. *Appl. Phys. A* **1998**, *66*, 659.
- (27) Rozhok, S.; Piner, R.; Mirkin, C. A. *J. Phys. Chem. B* **2003**, *107*, 751.
- (28) Increasing humidity to 80% does not significantly modify the size of the spots.
- (29) Zhang, L.; Macdonald, D. D.; Sikora, E.; Sikora, D. *J. Electrochem. Soc.* **1998**, *145*, 898.
- (30) Details of the procedure used to simulate the characteristics of the model, the various parameters K_i , R_j , R_C and R_S as well as the comments on the considered values for these parameters are given in Supporting Information Available.
- (31) Schneegans, O.; Moradpour, A.; Wang, K., manuscript in preparation.